This is a non-peer reviewed manuscript submitted to frontiers

A geothermal heat flow model of Africa based on Random Forest Regression

M. Al-Aghbary [1,2*], M. Sobh [1,3] and C. Gerhards [1]

[1]Institute of Geophysics and Geoinformatics, TU Bergakademie Freiberg, Germany
[2]Geophysical Laboratory, Centre d'Etudes et de Recherche de Djibouti, Djibouti
[3]National Research Institute of Astronomy and Geophysics (NRIAG), Helwan, Cairo, Egypt

Correspondence*:
Maged Al-Aghbary
Maged.Wahab@doktorand.tu-freiberg.de

ABSTRACT

We generate a geothermal heat flow model over Africa using random forest regression based on sixteen different geophysical and geological quantities (among them are Moho depth, Curie temperature depth, gravity anomalies, topography, and seismic wave velocities). The training of the random forest is based on direct heat flow measurements collected in the compilation of Lucazeau (2019). The final model reveals structures that are consistent with existing regional geothermal heat flow information. It is interpreted with respect to the tectonic setup of Africa, and the influence of the selection of training data and target observables is illustrated in the supplementary material.

Keywords: Geothermal Heat Flow, Random Forest Regression, Machine Learning, African continent

1 INTRODUCTION

Temperature gradients measured directly from boreholes are only sparsely available. Estimates of continental geothermal heat flow (GHF) can, therefore, only be derived indirectly from geophysical and geological quantities such as geomagnetic, seismic, gravity, topographic, and compositional data. This holds in particular for recent studies of Antarctica (e.g., Burton-Johnson et al. (2020); Lösing and Ebbing (2021); Stål et al. (2021)) but also for Africa, where advanced methods are required to incorporate sparse direct measurements with such indirect observables. Studies by He et al. (2022); Shahdi et al. (2021) compared several machine learning (ML) methods for geothermal heat flow modeling at regional scales and indicated that these methods can perform as good as, and sometimes better than, physics-based models. Physics-based models (such as, e.g., Lösing et al. (2020); Sobh et al. (2021)) often require various simplifications and are feasible only for few geophysical observables. Thus, if one wants to include several different geophysical and geological observables for the prediction of GHF, as seems necessary for continental scale models, purely physics-based models become unfeasible. Machine learning approaches for Greenland and Antarctica, both with very sparse direct GHF information, have been presented, e.g., in Lösing and Ebbing (2021); Rezvanbehbahani et al. (2017); Stål et al. (2021), with the former two publications using gradient boosted regression trees and the latter one a similarity detection approach. A random forest approach for modeling marine heat flow has been investigated in Li et al. (2022).

In this paper, we follow such a random forest approach to generate a GHF model for Africa, based on sixteen different geophysical and geological observables. Due to an intrinsic importance ranking of the random forest approach, we reduce the number of used observables to eleven for the final GHF model. An evaluation and interpretation of this model can be found in Section 4.

2 DATA AND GEOLOGICAL BACKGROUND

2.1 Geothermal Heat Flow Data

The New Global Heat Flow (NGHF) is a compilation of previous GHF databases containing 69,730 data points, with an average continental GHF of about 67 mWm^{-2} (Lucazeau, 2019). The NGHF rates the quality of the measurements as follows: A, B, C, D, and Z. To filter training data, we extract records with A and B ratings that correspond to less than 10% and less than 20% variation of GHF measurement in boreholes, respectively. As a result, the number of records is reduced to 12,707, with minimum and maximum values of -3.0 and 5,146.0 mWm^{-2}, respectively, and a mean of 66.1 mWm^{-2}. Furthermore, we exclude records from NGHF with missing spatial coordinates and missing GHF values. Additionally, we exclude records at high latitudes beyond -60° and 80°, respectively, and oceanic records (deeper than 1,000 m below sea level).

Exploratory data analysis revealed the presence of 62 measurements with GHF values over 200 mWm^2 inside the A labeled data and 113 measurement points over 200 mWm^2 inside the A and B labeled data. These values, together with negative values, are questionable and could be attributed either to some local thermal activities such as hydrothermal circulation or errors in measurements (Bachu, 1988). Hence, we exclude these values for our further continental-scale evaluations. As a result, we obtain a final dataset containing both A and B ratings. This GHF data will serve as our reference throughout the course of this paper. Additionally, we generate a reference dataset containing only A labeled data. Results for the latter data set can be found in the supplementary material. Figures 1(A and B) show density plots and the basic statistics of the eventually used data. Also, Figure 1(C) depicts the histogram of binned GHF measurements in Africa involving all records, records after removal of incomplete information, records after removal of deep-sea information, and records based on different quality ratings n the NGHF database.

2.2 Geological and Geophysical Data

We chose sixteen further geological and geophysical observables for the GHF model prediction, including global as well as regional datasets for Africa (see Table 1). They are of mixed types, categorical and continuous. For each observable to be considered, it should have a possible relation to GHF (please refer to Figure 2 for cross plots of the observables and GHF measurements). Our choice of observables and initial prepossessing steps are mostly adapted from Stål et al. (2021).

Global Moho and LAB depths are provided by the WINTERC-G model from Fullea et al. (2021). Global Curie temperature depth (CTD) is obtained from Gard and Hasterok (2021). Upper mantle velocity models may shed light on the mantle and lithospheric components of the GHF (Shapiro and Ritzwoller, 2004). S-wave velocities are derived from the global model SL2013sv, and the African regional model AF2019 is obtained from (Schaeffer and Lebedev, 2013) and (Celli et al., 2020b), respectively. The global P-wave velocity model, DETOX-P1, and the African regional

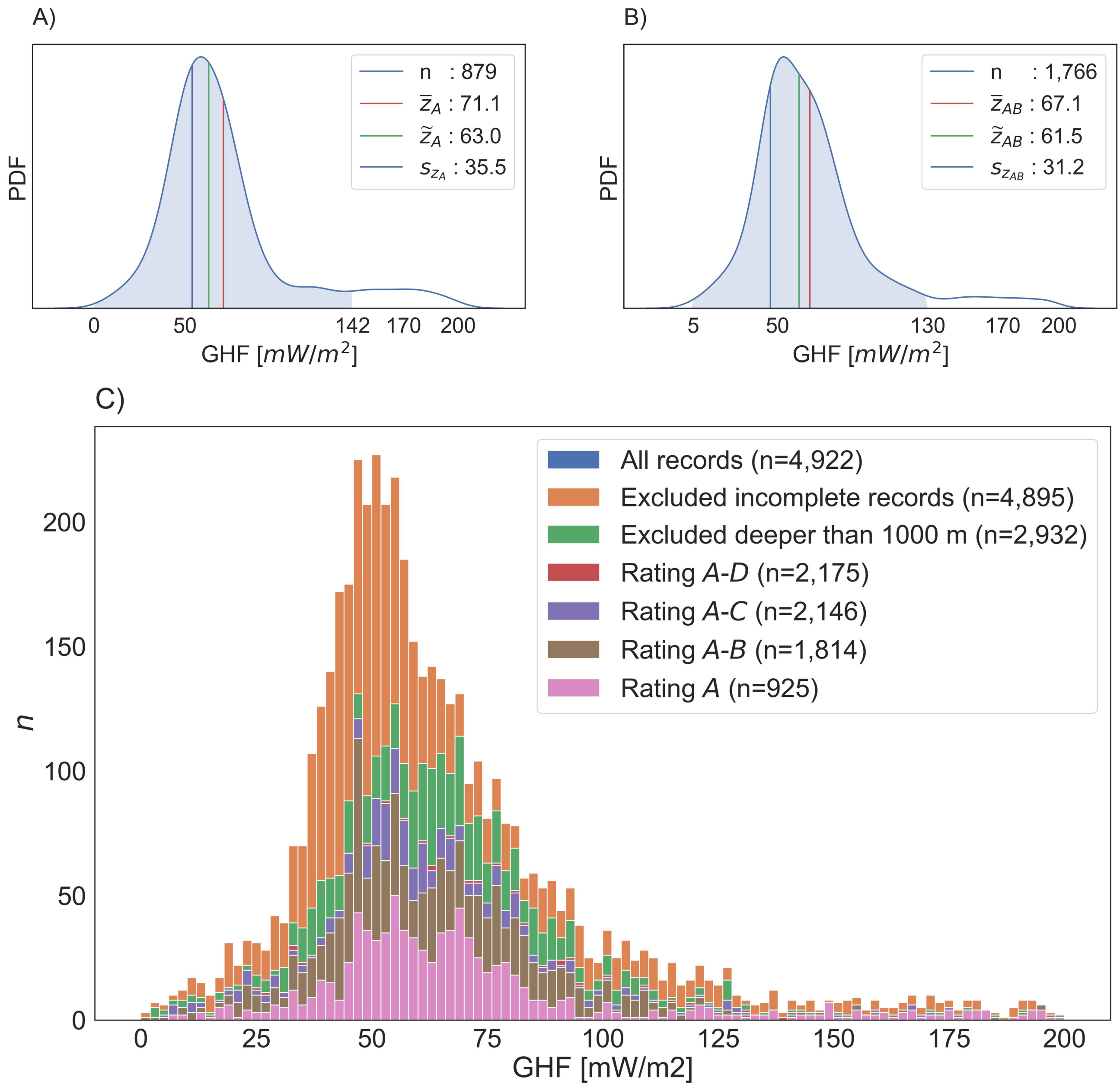

Figure 1. (A) Density plot of GHF measurements in Africa labeled *A* without questionable values, (B) Density plot of GHF measurements in Africa labeled *A* and *B* without questionable values, (C) Histogram of binned GHF measurements in Africa involving all records, records after removal of incomplete information, records after removal of deep-sea information, and records based on different quality ratings n the NGHF database. (Lucazeau, 2019). $\bar{z}$ = mean, $\tilde{z}$ = median, s = standard deviation.

model, AFRP20, are obtained from (Hosseini et al., 2020) and (Boyce et al., 2021). In our set of observables, we consider the P- and S-wave velocities at a depth of 150 km. The Digital Elevation Model (DEM), which represents the topography in m, is obtained from ETOPO1 (Amante and Eakins, 2009). ETOPO1 is a global relief model of the Earth's surface with 1-arcminute resolution. The average densities of the crust and lithosphere in kg/m^{-3} are obtained from the LithoRef18 (Afonso et al., 2019) model. We used the EMAG2v3 geomagnetic anomaly map in nT from (Meyer et al., 2017). EMAG2v3 is a global grid of geomagnetic anomalies compiled from satellite, shipboard,

Table 1. The observables used in this study with their sources, number of records and range

	observable	Source	Records	Range
1	$Moho\,Depth$	(Fullea et al., 2021)	12,232	(11, 67)
2	$LAB\,Depth$	(Fullea et al., 2021)	12,232	(61, 300)
3	$Global\,S_v\,velocity$	(Schaeffer and Lebedev, 2013)	260,281	(-0.078, 0.095)
	$African\,S_v\,velocity$	(Celli et al., 2020b)	28,497	(-0.078, 0.095)
4	$Global\,P_v\,velocity$	(Hosseini et al., 2020)	260,281	(-0.025,0.02)
	$African\,P_v\,velocity$	(Boyce et al., 2021)	124,609	(-0.025,0.02)
5	$Global\,CTD$	(Gard and Hasterok, 2021)	65,341	(15, 74)
6	$Geomagnetic\,Anomaly$	(Meyer et al., 2017)	1,257,502	(-1, 0.7)
7	DEM	(Amante and Eakins, 2009)	1,257,502	(-5140, 5109)
8	$Lithosphere\,Density$	(Afonso et al., 2019)	16,200	(3260, 3360)
9	$Crustal\,Density$	(Afonso et al., 2019)	16,200	(2650, 2950)
10	$Free-air\,Anomaly$	(Förste et al., 2013)	65,340	(-0.18, 0.26)
11	$Geoid\,Height$	(Förste et al., 2013)	65,341	(-96, 67)
12	$Bouguer\,Anomaly$	(Ince et al., 2019)	65,341	(-0.55, 0.33)
13	$Shape\,Index$	(Ebbing et al., 2018)	1,618,201	(-1 , 1)
14	$Tectonic\,Regions$	(Schaeffer and Lebedev, 2015)	16,472	(1, 6)
15	$GLiM$	(Gard et al., 2019)	1,257,502	(1, 16)
16	$Distance-to-Volcano$	(Siebert et al., 2015)	2,652	(0, 1)
17	$NGHF\,(A)$	(Lucazeau, 2019)	5,792	(6 , 197)
	$NGHF\,(A \text{ and } B)$	(Lucazeau, 2019)	12,707	(1 , 197)

and airborne magnetic measurements at 2-arcminute resolution. Due to the variation of geomagnetic anomaly data over several orders of magnitude, we transformed it via $M_{\log} = \mathrm{sgn}(M)\ln(1 + M/400)$ and clipped it to the interval $[-1, 1]$, where M is the original geomagnetic anomaly data and $M_{\log}$ the transformed quantity that we use in the course of this paper. The four observables that reflect gravity information are derived from the EIGEN-6C4 model (Förste et al., 2013). Calculations of the geoid in m, free-air gravity, and Bouger gravity in mGals are performed by ICGEM (Ince et al., 2019). We also include the gravity field curvature shape index (Ebbing et al., 2018) derived from the two horizontal and independent components of the satellite gravity gradient from GOCE data (Pail et al., 2010). This is a dimensionless quantity with an interval of $[-1, 1]$.

The proximity to the nearest young volcanoes is calculated from the Global Volcanism Program (Siebert et al., 2015). Since the volcanoes belong to the Holocene and Pleistocene epochs, this observable is a useful indicator of high GHF. The distances between our target locations and a specific volcano is computed along great circles and this distance is then transformed via $1 - (\text{dist}/100)$ and clipped to a unitless range of $[0, 1]$. Volcanoes farther away than 100 km from the specific target location are excluded. We also included categorical data on lithologies and tectonic regions. The global lithology map (GLiM) database was compiled by (Gard et al., 2019). It groups the surface lithologies into sixteen classes. As for the tectonic regionalization, the model proposed by (Schaeffer and Lebedev, 2015) delineates six tectonic regions.

We choose the IsolationForest routine (Liu et al., 2008; Buitinck et al., 2013) to detect outliers in the data described above. Those removed outliers are depicted as red points in Figure 2. The Pearson correlation matrix for the given observables before and after deleting the outliers are provided in

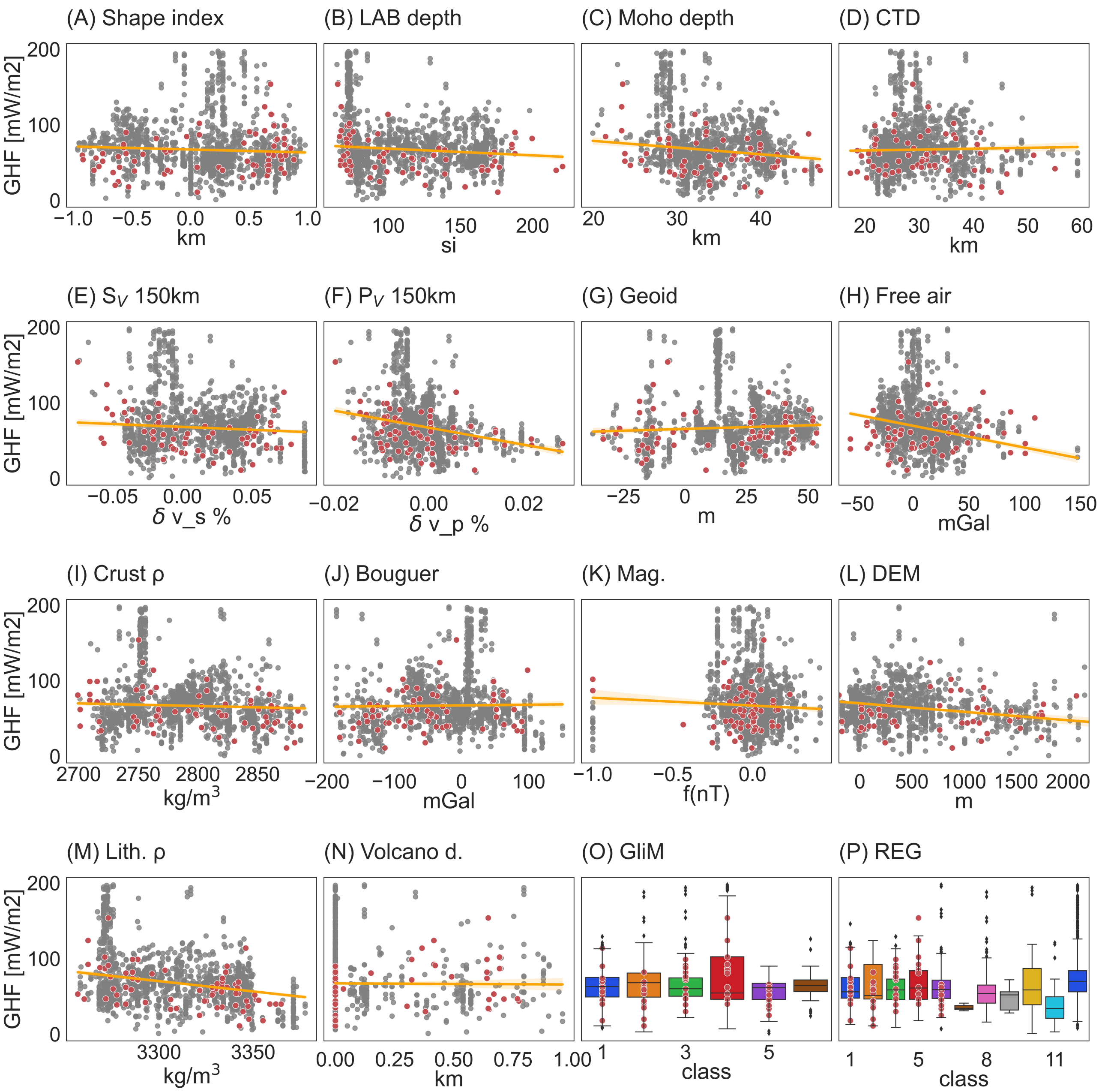

Figure 2. Cross plots of the geological and geophysical observables against GHF measurements; the orange lines indicate the linear regression results. Categorical observables are illustrated by boxplots. Red dots indicate outliers.

Figures S3 and S4 in the supplementary material. Figure 3 illustrates those observables that have eventually been used for the generation of the GHF model presented in this paper. The remaining observables have been neglected due to an importance ranking described later on in Section 3.3.

2.3 Gridding of the Data

We imported the previously described observables and stacked them into a multi-dimensional grid using Agrid (Stål and Reading, 2019). We generate a grid of $0.5° \times 0.5°$ resolution. In grid cells where no data for the geological or geophysical observable under consideration is available or where the resolution of the original data is not sufficient, we interpolate via inverse distance weighting

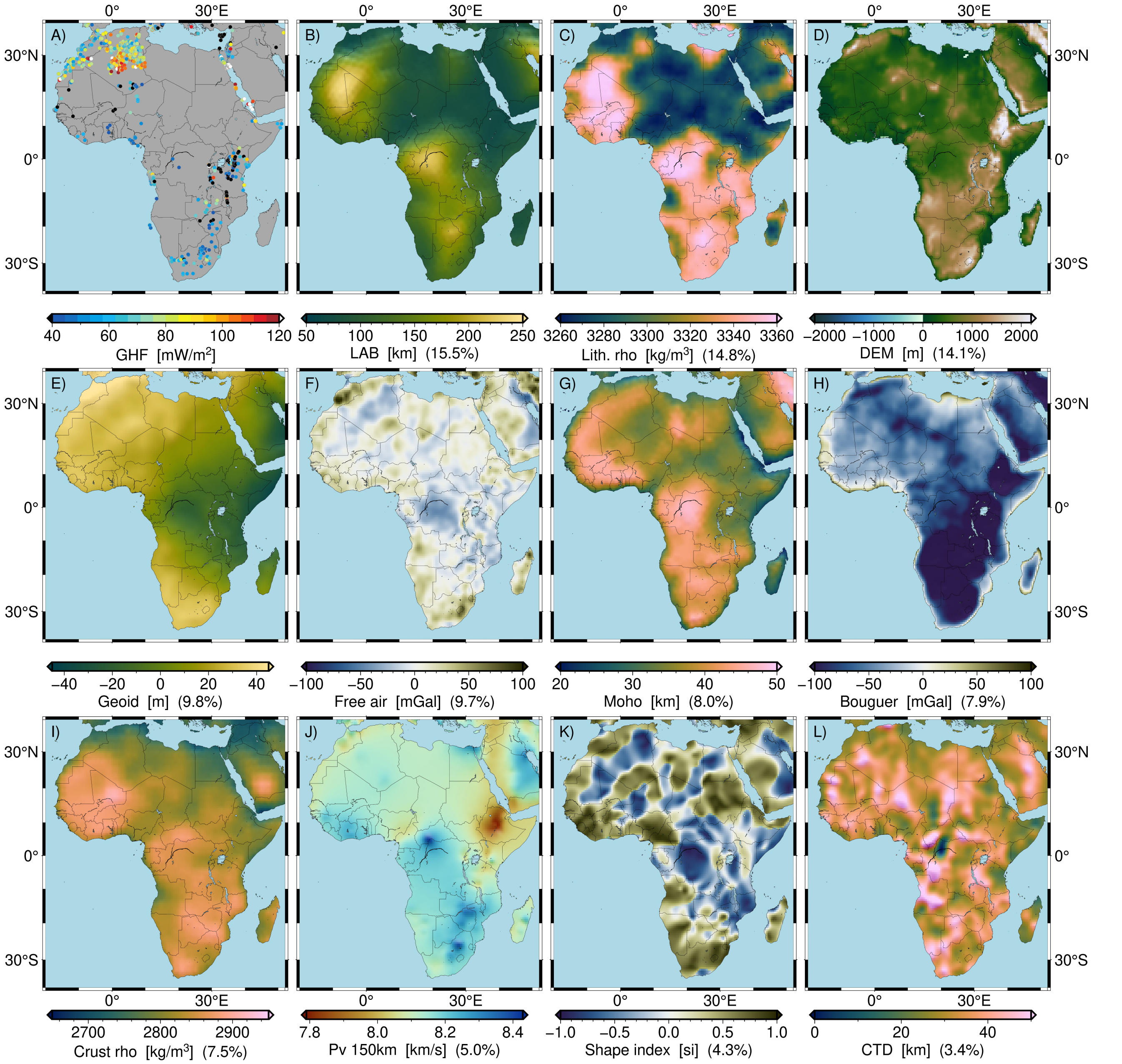

Figure 3. Illustration of the observables used in this study: (A) measured GHF, (B) Lithosphere–Asthenosphere Boundary (LAB) depth (C) Lithospheric average density, (D) Digital Elevation Model (DEM), (E) Geoid, (F) Free-air gravity anomaly, (G) Moho depth, (H) Bouguer anomaly, (I) Crustal average density, (J) P_v velocity, (K) Shape index, (L) Curie temperature depth. The percentages in brackets represent the relative importance of each target observable, as described later on in Section 3.3

(IDW) if the observable is of continuous type. The samples of the GHF data described in Section 2.1 are not interpolated but simply reassigned to the grid cells nearest to the sample locations. In the course of the paper, we refer to the samples at grid cells where GHF data is available as reference data (including GHF as well as all further geological and geophysical observables). All samples at grid cells where no GHF information is available are denoted as target data (including all geological and geophysical observables other than GHF). These are the locations at which we want to predict GHF values.

2.4 Geological Background of Africa

The African continent is composed mainly of Precambrian terranes, assembled in the Late Neoproterozoic-Early Paleozoic Pan-African orogeny (Begg et al., 2009). Confer Figure 4 for an illustration. Three major cratons identified in Africa are the West African, Congo and Kalahari Cratons, with the smaller Tanzanian Craton located east of Congo, and Saharan Metacraton at the North (Sobh et al., 2020)). The greater Kalahari Craton consists of Kaapvaal and Zimbabwe cratons

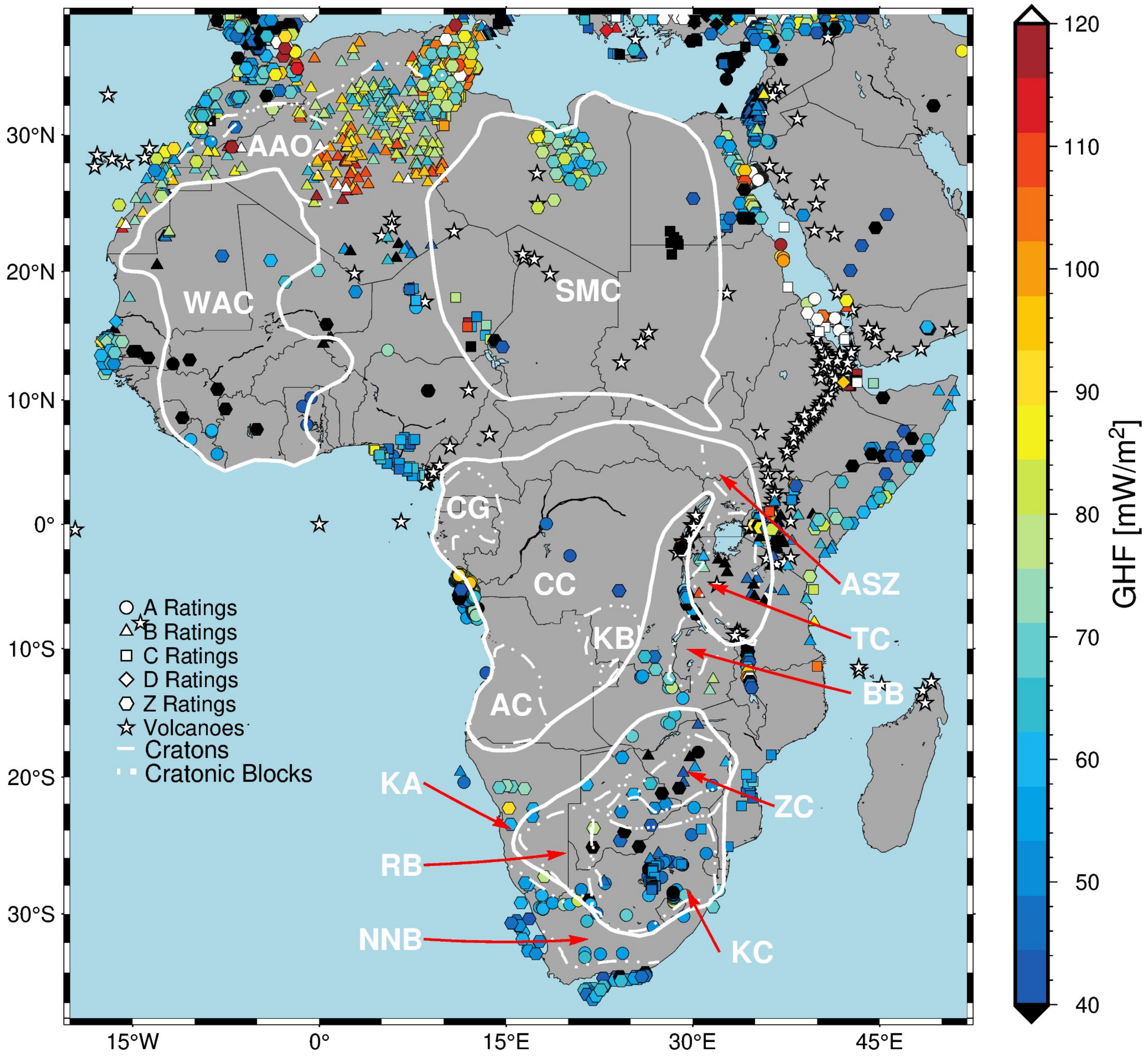

Figure 4. Simplified tectonic map of Africa with Cratons, Cratonic blocks, and other relevant tectonic units. Cratons are plotted in white polygons, KA = Kalahari Craton; CC = Congo Craton; WAC = West African Craton; SMC = Saharan Metacraton. Cratonic blocks: BB = Bangweulu Block; ZC = Zimbabwe Craton; TC = Tanzanian Craton; KC = Kaapvaal Craton; AC = Angola Craton; KB = Kasai Block; GC = Gabon–Cameroon Block. RB = Rehoboth Block; NNB = Namaqua-Natal Belt; ASZ = Aswa Shear Zone. Symbols of circle, triangle, square, diamond and hexagon represent the Reference GHF with A, B, C, D and Z ratings respectively, derived from global compilation of GHF database (Lucazeau, 2019). White asterisks = Volcanoes.

separated by the Limpopo Belt (de Wit et al., 1992) and the Rehoboth basin (Muller et al., 2009) to the west. The Congo Craton in central Africa hosts three Archean shield areas, parts of which are probably covered by the Congo basin: the Gabon-Cameroon (GC) in the Northwest, Kasai block (KB) in the central East, and Angolan craton (AC) along the western border south of the Gabon Cameroon (Celli et al., 2020a).

Toward Northern Africa, the West African Craton (WAC) and the Saharan Metacraton (SMC) are separated by the West African Mobile Zone (WAMZ). In the Cenozoic, widespread volcanism affected the African continent, mainly related to Pan-African crustal reactivation (Ashwal and Burke, 1989), continental rifting (Thorpe and Smith, 1974), hotspots (e.g., Hoggar, Tibesti, Darfur and Cameroon Volcanic Line), and the East African Rift System (EARS). The EARS is a seismically and volcanically active rift system (Sengör and Burke, 1978), whose geodynamic origin is under debate. Some studies support the origin of EARS as plume origin; Afar plume (Ebinger et al., 1989) or multiple plumes (Rogers et al., 2000) or even connection to the African Superplume (Hansen and Nyblade, 2013). The EARS is formed of Eastern and Western Branches. The Eastern Branch is a volcanic reach system consisting of Afar and Main Ethiopian Rifts. The Western Branch is younger with less volcanic activity (Ebinger et al., 1989).

3 METHODOLOGY

3.1 Random Forest Regression

A random forest (RF) is a collection of decision trees T, with each tree being able to provide a separate GHF prediction for the set of target observables $\mathcal{T}$. Each tree within the forest is build from a subset of the available reference observables $\mathcal{R}$, where each subset contains information on at most P randomly chosen observables (among the sixteen available observables). Furthermore, by D we denote the maximum possible depth of each tree, by S the minimum number of samples required in a leaf node of a tree, and by K the required minimum number of samples in an internal node of a tree in order to allow a further split this node. We call $\mathbf{h} = (T, P, D, S, K)$ the hyperparameters of the RF. Once a RF is built for a certain set of hyperparameters, the predicted GHF value is obtained by averaging over the separate predictions of all T decision trees. The GHF model obtained this way will be denoted by AFQ. A detailed description of the concept of RF regression can be found in the original publication Breiman (2001).

3.2 Training the Random Forest

To clarify the procedure, we denote by $\mathcal{R} = \{(z_n^{\mathrm{r}}, \mathbf{y}_n^{\mathrm{r}}) : n = 1, \ldots, N\}$ the set of reference observables $\mathbf{y}_n^{\mathrm{r}}$ (cf. Section 2.2; each $\mathbf{y}_m^{\mathrm{r}}$ contains sixteen entries covering the available observables) and corresponding reference GHF values z_n^{r} (cf. Section 2.1; for our model we only use reference samples located within the African continent). The set of target observables is denoted by $\mathcal{T} = \{\mathbf{y}_m^{\mathrm{t}} : m = 1, \ldots, M\}$, comprising the observables described in Section 2.2 at locations where no GHF infpormation is available. In order to train the RF, we choose a training subset of $\mathcal{R}$ that contains 80% of the reference samples, leaving the remaining 20% as an out-of-bag set for a possible later visual validation of the training result. From the training subset we then use 90% of the samples for actually building the RF and the remaining 10% for cross-validation, resulting in N_{cv} samples for cross-validation (this procedure is iterated for ten different random choices of subsets). The optimal hyperparameters $\mathbf{h}$ are chosen by minimizing the mean square error (MSE)

$$\mathrm{MSE}(\mathbf{h}) = \frac{1}{N_{\mathrm{cv}}} \sum_{i=1}^{N_{\mathrm{cv}}} \left| z_i^{\mathrm{r}} - \hat{z}_{i,\mathbf{h}}^{\mathrm{RF}} \right|^2, \tag{1}$$

where z_i^{r} denotes the available reference GHF in the cross-validation subset, and $\hat{z}_{i,\mathbf{h}}^{\mathrm{RF}}$ denotes the corresponding GHF predicted by the trained RF for the particular hyperparameters $\mathbf{h}$. For the numerical implementation of this RF approach, we use the code provided by Sklearn (Buitinck et al., 2013) and Scikit-Optimize (Head et al., 2018). The initial GHF model then comprises the GHF values $\hat{z}_{m,\mathbf{h}}^{\mathrm{RF}}$ predicted for the target observables $\mathbf{y}_m^{\mathrm{t}}$ in $\mathcal{T}$, using the trained RF with optimized hyperparameters $\mathbf{h}$.

3.3 Observable Selection

Related decision tree based methods have been used, e.g., in (Lösing and Ebbing, 2021; Rezvanbehbahani et al., 2017) for the prediction of GHF. However, in the gradient boosted setup used in these references, the trees are generated iteratively and require a regularization term to prevent overfitting while in the RF setup, the trees can be computed in parallel and overfitting is prevented by the random selection of observables for each tree and the eventual averaging of the predictions over all trees. What both ensemble methods have in common is that they can provide the user with an importance ranking of the involved observables. The importance is based on the reduction of variance of an observable at a splitting node of a tree. After ranking all sixteen observables, recursive feature elimination with cross-validation (RFECV) is used to iteratively delete the least important feature and check certain performance indicators of the random forest obtained from this reduced number of observables (Guyon et al., 2002). This supports the decision on how many and which features to use for the generation of the eventual RF. Figure 8 shows the obtained importance ranking for our setup and it also indicates the performance indicators NRMSe and R^2 obtained during RFECV. Again, for the implementation we use Sklearn (Buitinck et al., 2013). For the final GHF produced in this paper, as shown in Section 4, we use only the eleven most important observables. This final model we call AFQ and it will be the one presented in the main body of this paper. GHF models relying on a different number of observables and training data can be found in the supplementary material for comparison.

3.4 Model Uncertainty

As described before in Section 3.3, we only present the GHF model built from the eleven most important observables. However, we use all obtained GHF models based on reference GHF data labeled A and B (including those shown in the supplementary material; altogether this amounts to twelve models) to compute the quantity

$$\mathrm{ran}(x_m^{\mathrm{t}}) = \frac{\max_i \mathrm{AFQ}^i(x_m^{\mathrm{t}}) - \min_i \mathrm{AFQ}^i(x_m^{\mathrm{t}})}{2}, \tag{2}$$

which captures the range among these models at the target location x_m^{t} (by AFQ^i we denote the model based on the i most important observables according to the ranking in Figure 8). Later on, we refer to this quantity as uncertainty, although it should clearly not be considered a statistically proper definition of uncertainty: in particular, the range defined in (2) only captures variations due to the number of included observables, not due to noise in the data (this has been tried to be reduced by a proper data selection) nor due to sampling bias (i.e., an insufficient representation of the geology at the target location by the training data).

4 RESULTS AND DISCUSSION

We present the modeled GHF together with the associated uncertainties. Additionally, we provide an evaluation of the modeled GHF and its geological implications.

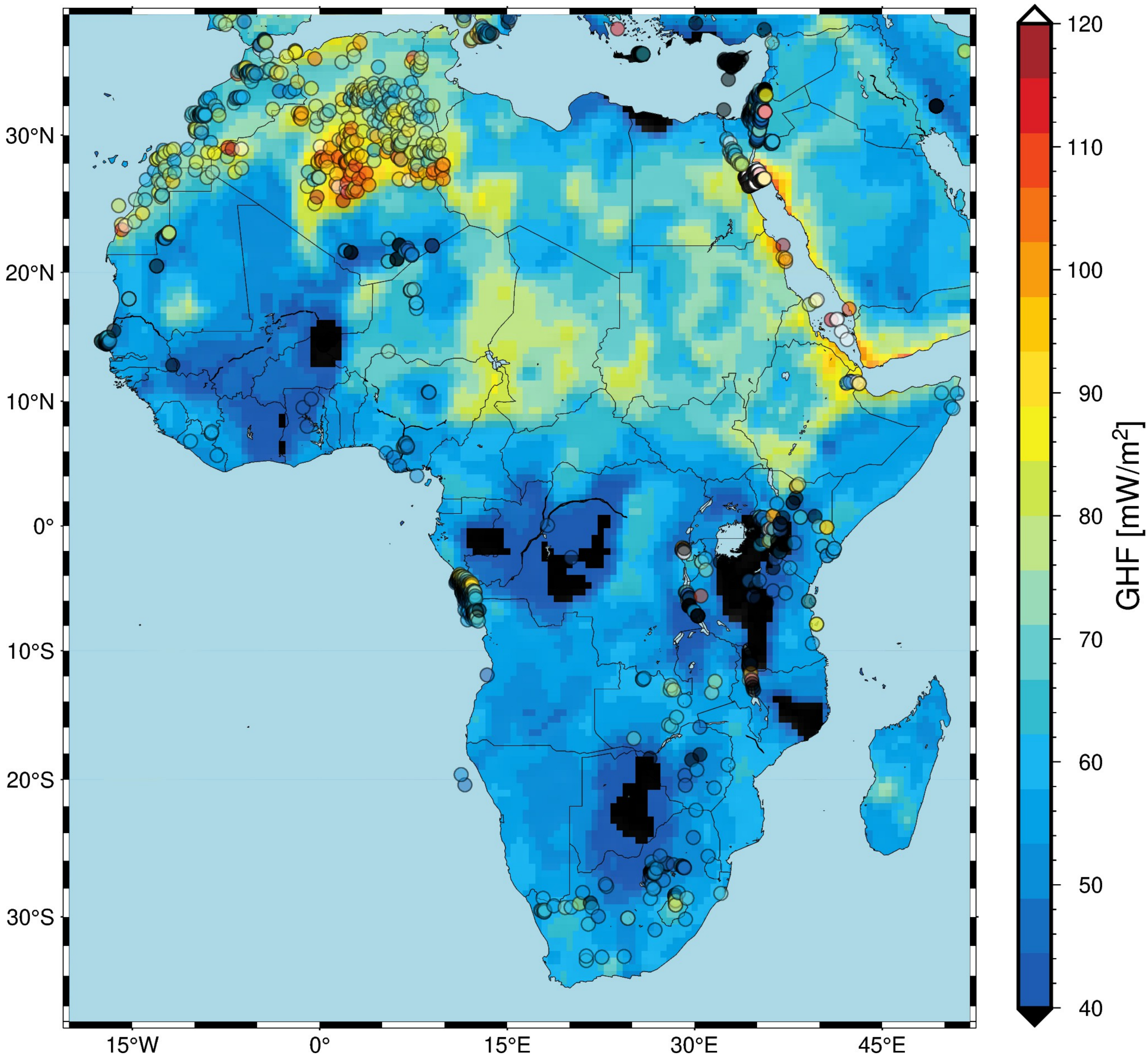

Figure 5. Modeled GHF of Africa based on eleven observables (AFQ), overlain with the locations of the reference GHF data.

4.1 The GHF model over Africa

Figure 5 shows the predicted GHF for Africa based on a random forest trained with the eleven most important observables (according to the importance ranking from Figure 8) and GHF reference data labeled A and B. Figures S5 and S6 in the supporting material show various alternative versions of AFQ, trained with reference data containing samples labeled A and B as well as with reference data containing only samples labeled A. Comparing the models trained solely with GHF data labeled A to those trained with data labeled A and B, it becomes obvious that the models only trained with A labeled data do not capture the high GHF zone in Algeria (which is covered mostly by B labeled reference data). This underlines the expectation that the capability of generalization of the trained RF strongly depends on the training data, the so-called sampling bias. In this case it would suggest that the geological and geophysical situation in Algeria is different from the areas where A labeled GHF data is available. Please refer to Figure S8 in the supporting material for a GHF model that also covers the oceanic parts.

4.2 Model Evaluation

Figure 6(A) indicates that the agreement of AFQ with direct measurements is generally good with a NRMSe of 0.22. Also, the R^2 value of 0.77 indicates a good fit. In average, the AFQ model overestimates GHF values by 5.1%. Figure 6(B) shows the density plots of reference values and predicted values of AFQ. The model reveals a certain inability to predict high GHF values. Hence its standard deviations is lower than that of the reference GHF data. Also Figure 6(A) shows that for high values (> 125 mWm^2) the model's predictions become more unstable. This could be due to an underrepresentation of such high values in the training dataset, amounting to only 5.5% of the training data (i.e., 95 samples).

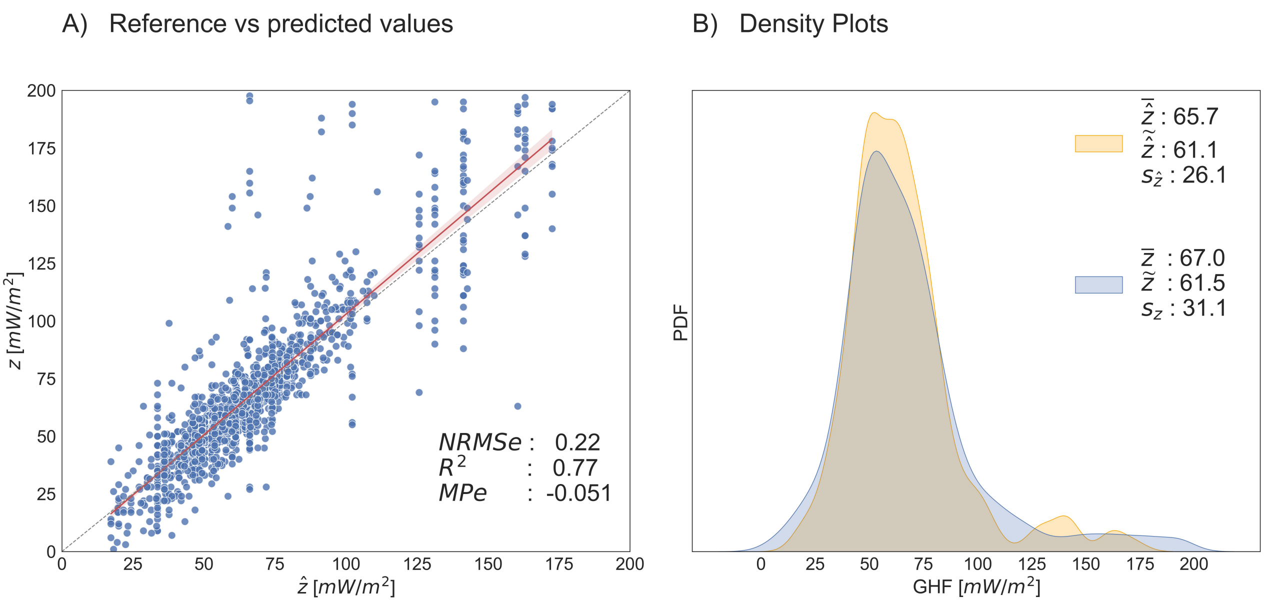

Figure 6. Performance indicators for the GHF model over Africa (AFQ): (A) Scatter plot of reference vs predicted values, (B) probability density plot of reference and predicted values.

4.3 Model Uncertainties

Figure 7(A) shows the quantity $\mathrm{CV}(x^{\mathrm{t}}_m) = \left|\mathrm{AFQ}(x^{\mathrm{t}}_m) - \overline{\mathrm{AFQ}}\right| / \overline{\mathrm{AFQ}}$, similar to the common Coefficient of Variation at the target location x^{t}_m. In regions without available reference GHF data, elevated CV values might indicate that AFQ actually “predicts” geothermal heat flow (based on the underlying trained random forest) and not just “averages” to a global mean. This is the case, e.g., in the Gabon craton, northern Egypt, and western and southern Arabia. However, in contrast to this, there also exist various regions that are lacking reference GHF data and which reveal low CV values, i.e., the predicted value is close to the global mean. In those cases, it is difficult to distinguish if this is due to the lack of reference GHF information in these regions or if these values actually reflect valid geological information.

Figure 7(B) shows the model uncertainty based on the range (2) among GHF models trained with different numbers of observables. AFQ reveals high uncertainties in central and northwestern parts of Africa as well as in parts of the Middle East. One can observe that these areas of increased uncertainty correlate with areas lacking reference GHF information or areas covered mainly by reference values labeled B, e.g., in Algeria. They seem to be particularly affected by the choice of target observables.

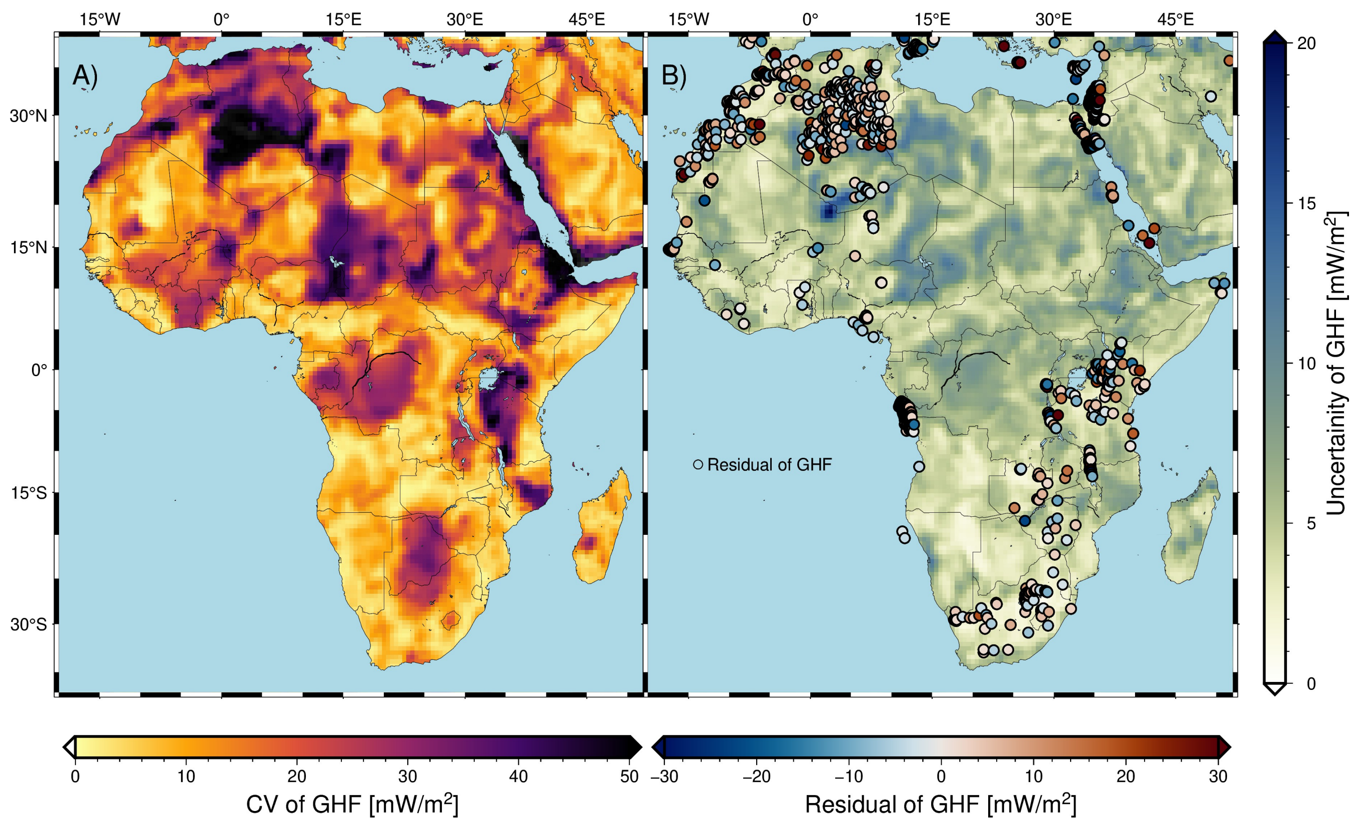

Figure 7. Uncertainties for AFQ: (A) Coefficient of Variation for AFQ, (B) Uncertainty of AFQ given by the range defined in (2). The residuals between reference and predicted values are overlaid as circles.

4.4 Interpretation

GHF is known to be broadly correlated with the tectonic setting of a region (Jaupart et al., 2007). The GHF model shown in Figure 5 indicates large-scale low-heat flow regions associated with the more stable tectonic regimes (e.g., KC; CC; and TC). Such results are highly consistent with the seismic tomographic results, showing high-velocity values in the upper mantle in these areas (Fishwick and Bastow (2011); Emry et al. (2019); Celli et al. (2020a)).

High GHF values are seen most clearly in the most active tectonics parts (e.g., EARS). Underneath the EARS, pronounced high-heat flow extends from Afar in the north to Tanzania in the south. EARS is considered as a remarkable geothermal potential in Africa due to geothermal sources related to magmatism and volcanism along the rift axis. There is much more variability in our model in the western branch compared to the eastern branch. In general, GHF values decrease away from the EARS. Recent seismic tomography studies inferred a significant mantle velocity reduction of the S-wave velocity in regions of Cenozoic volcanism due to thinning of the lithosphere (Fishwick and Bastow (2011); Emry et al. (2019); Celli et al. (2020a); Sobh et al. (2020)).

Moderate to high GHF exists in northern Morocco, where GHF values partially exceed 100 mWm^2. This is in agreement with the results of (Rimi, 2000). Similar high GHF values (> 80 mWm^2) are present in a large area of western Algeria. Heat flow in this area has been previously modeled by (Lesquer and Vasseur, 1992). Along the West African Rift System (WARS) in the northeast of Nigeria the modeled GHF values are > 90 mWm^2, which has been recorded also in Kwaya et al. (2016). Beneath the Darfur hot spot, our model correctly predicts high GHFs. This is also the case along the Tibesti volcanic region, however, with lower values.

A physics-based geothermal heat flow map of Southern Africa obtained from a single observable (namely, the Curie depth as inverted from magnetic anomaly information) has been presented in Sobh et al. (2021). It is notable that the multi-observable based model AFQ presented here predicts lower heat flow along South African cratonic blocks (KC and ZC), while the model by Sobh et al. (2021) exhibits very high heat flow regions especially in the Kalahari Magnetic Lineament.

4.5 Comments on the choice of observables

As black-box techniques, ML algorithms are often faced with issues of interpretability. An example of that in this paper is the given relatively high importance of DEM (i.e., the topography) with 14.1% in the final model (please refer to Figure 8). The high ranking could be explained by an internal mechanism where DEM correlates well with another observable, leading to it being ranked higher at the expense of this correlated observable. As another example, distance to the nearest volcanoes should intuitively be a good indicator of GHF (as is the case, e.g., in Lösing and Ebbing (2021)), however, it was ranked lower. This could be explained mainly due to the sparsity of this observable, where most of the values are zero due to the distance to the next volcano being > 100 km. In addition, despite the importance of Curie temperature depth, geomagnetic anomalies, GLiM, and tectonic regionalization as observables in other studies, their contribution in this study are significantly less. Please refer to the supplementary material Figure S6 for a comparison between models trained with those observables and the current model trained without them. They indicate that, in fact, the inclusion of these additional observables does not significantly affect the GHF model. Thus, we opted to present only the model trained with the eleven most important features in this paper.

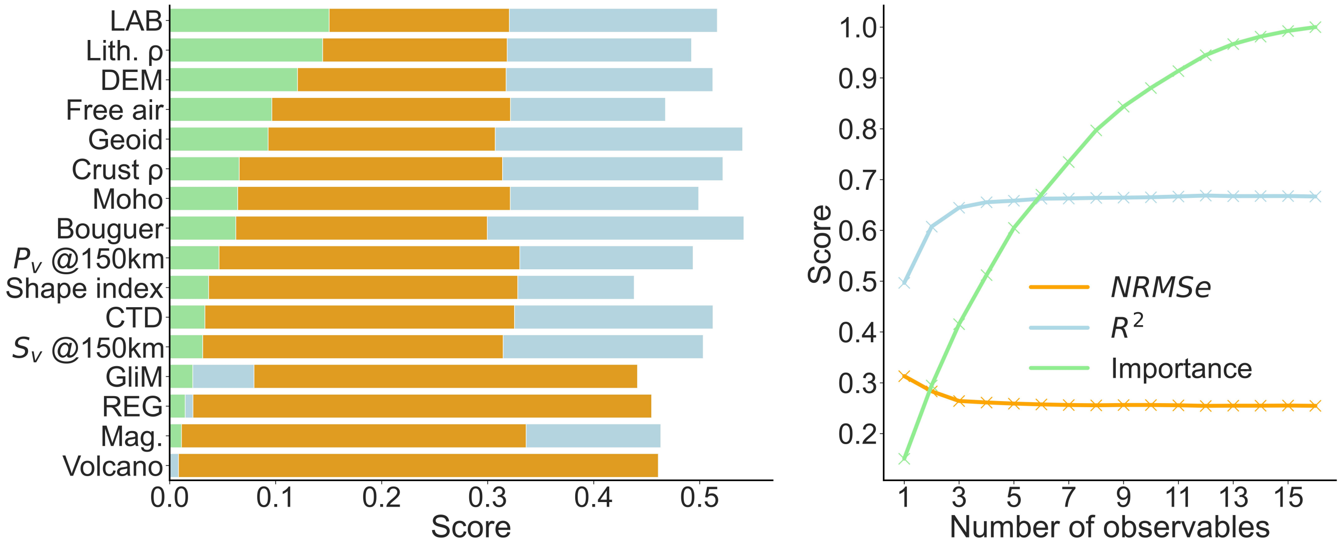

Figure 8. (A) Relative importance of the observables together with their coefficient of determination R^2, and normalized root mean square error NRMSe ranked by their contribution to the RF prediction, (B) Scores for cumulative sum of relative importance, R^2, and NRMSe with increasing number of observables.

5 CONCLUSION

The objective of this paper is to present the geothermal heat flow model AFQ over Africa, based on RF regression. All in all, AFQ trains with the eleven most important observables among sixteen available observables that cover various geophysical and geological properties at a resolution of $0.5° \times 0.5°$. In agreement with available geological and GHF information, AFQ shows elevated GHF around the red sea and along the east and west African rift systems, low GHF values around major cratons as well as cratonic blocks, and intermediate values elsewhere.

However, we want to mention that the RF approach used here, as well as the machine learning approaches used in other publications mentioned throughout this paper, are solely based on similarity structures between the different samples of geological and geophysical observables. They do not reflect spatial correlations of the observables. The latter will be an interesting task, together with a proper uncertainty quantification, for future work.

NOMENCLATURE

AFQ	African Heat Flow Model
GHF	Geothermal Heat Flow
NGHF	New Global Heat Flow database
NRMSe	Normalized Root Mean Square Error
R^2	Coefficient of Determination
RF	Random Forest

PERMISSION TO REUSE AND COPYRIGHT

CONFLICT OF INTEREST STATEMENT

The authors declare that the research was conducted in the absence of any commercial or financial relationships that could be construed as a potential conflict of interest.

AUTHOR CONTRIBUTIONS

The authors confirm their contribution to the paper as follows: study conception, design, and data collection: M. Al-Aghbary; analysis and interpretation of results: M. Al-Aghbary, M. Sobh; revision and supervision: M. Sobh, C. Gerhards. All authors reviewed the results and contributed to the draft and final version of the manuscript.

ACKNOWLEDGMENTS

This work has been partially funded by BMWi (Bundesministerium für Wirtschaft und Energie) within the joint project 'SYSEXPL – Systematische Exploration', grant ref. 03EE4002B, and Centre d'Etudes et de Recherche de Djibouti (CERD).

DATA AVAILABILITY STATEMENT

The observables used in this study can be found in the following online repositories: (a) Moho and LAB Depths, (Fullea et al., 2021), https://www.3dearth.uni-kiel.de/en/public-data-products/public-data-products, (downloaded 01.08.2021). (b) S-wave velocity, (Schaeffer and Lebedev, 2013), https://www.earth.ox.ac.uk/~smachine/cgi/index.php?page=tomo_depth, (downloaded 01.08.2021). African S-wave velocity, (Celli et al., 2020b), https://nlscelli.wixsite.com/ncseismology/af2019, (downloaded 01.08.2021). (c) P-wave velocity, (Hosseini et al., 2020), https://www.earth.ox.ac.uk/~smachine/cgi/index.php?page=tomo_depth, (downloaded 01.08.2021). African P-wave velocity, (Boyce et al., 2021), http://ds.iris.edu/ds/products/emc-afrp20/, (downloaded 01.08.2021). (d) Curie Temperature Depth, (Gard and Hasterok, 2021), https://data.mendeley.com/datasets/bvz2jz99xh/2, (downloaded 10.08.2021). (e) Geomagnetic Anomaly, (Meyer et al., 2017), https://doi.org/10.7289/V5H70CVX, (downloaded 10.08.2021). (f) Elevation, (Amante and Eakins, 2009) https://www.ngdc.noaa.gov/mgg/global/relief/ETOPO1/data/bedrock/grid_registered/georeferenced_tiff/, (downloaded 10.08.2021). (g) Lithosphere and Crustal Average Density, (Afonso et al., 2019), https://www.juanafonso.com/software, (downloaded 10.08.2021). (h) Geoid Height, Free Air and Bouguer Anomalies, (Förste et al., 2013), http://icgem.gfz-potsdam.de/calcgrid, (downloaded 15.08.2021). (i) Shape Index of Curvature, (Ebbing et al., 2018), https://www.3dearth.uni-kiel.de/en/public-data-products/copy_of_depth-to-moho-boundary, (downloaded 15.08.2021). (j) Distance-to-Volcano, (Siebert et al., 2015), https://volcano.si.edu/volcanolist_holocene.cfm and https://volcano.si.edu/volcanolist_pleistocene.cfm, (downloaded 15.08.2021). (k) Tectonic Regionalization, (Schaeffer and Lebedev, 2015), https://schaeffer.ca/models/sl2013sv-tectonic-regionalization/, (downloaded 18.08.2021). (l) Global Lithological Map, (Gard et al., 2019), https://doi.pangaea.de/10.1594/PANGAEA.788537, (downloaded 18.08.2021). (m) NGHF, (Lucazeau, 2019), https://doi.org/10.1029/2019GC008389, (downloaded 18.08.2021).

Softwares used in this study are available at: (a) Agrid, (Stål and Reading, 2019), http://doi.org/10.5334/jors.287, (downloaded 20.08.2021). (b) sklearn, (Buitinck et al., 2013), https://arxiv.org/abs/1309.0238, (downloaded 20.08.2021). (c) Pandas, (pandas development team, 2020), https://doi.org/10.5281/zenodo.3509134, (downloaded 20.08.2021). (e) Seaborn, (Waskom, 2021), https://doi.org/10.21105/joss.03021, (downloaded 20.08.2021). (e) scikit-optimize, (Head et al., 2018), https://doi.org/10.5281/zenodo.1207017, (downloaded 10.09.2021). (f) Pygmt, (Uieda et al., 2021), https://zenodo.org/record/5607255, (downloaded 10.09.2021). (g) Numpy, (Harris et al., 2020), https://doi.org/10.1038/s41586-020-2649-2, (downloaded 10.09.2021). (h) Scipy, (Virtanen et al., 2020), https://doi.org/10.1038/s41586-020-2649-2, (downloaded 10.09.2021).

The script and data generated in this study can be found here: AFQ, https://doi.org/10.5281/zenodo.6780402

REFERENCES

Afonso, J. C., Salajegheh, F., Szwillus, W., Ebbing, J., and Gaina, C. (2019). A global reference model of the lithosphere and upper mantle from joint inversion and analysis of multiple data sets. Geophysical Journal International 217, 1602–1628. doi:https://doi.org/10.1093/gji/ggz094

Amante, C. and Eakins, B. W. (2009). Etopo1 1 arc-minute global relief model: procedures, data sources and analysis. noaa technical memorandum nesdis ngdc-24. National Geophysical Data Center, NOAA 10, V5C8276M. doi:doi:10.1594/PANGAEA.104840

Ashwal, L. D. and Burke, K. (1989). African lithospheric structure, volcanism, and topography. Earth and Planetary Science Letters 96, 8–14

Bachu, S. (1988). Analysis of heat transfer processes and geothermal pattern in the alberta basin, canada. Journal of Geophysical Research: Solid Earth 93, 7767–7781

Begg, G., Griffin, W., Natapov, L., O'Reilly, S. Y., Grand, S., O'Neill, C., et al. (2009). The lithospheric architecture of africa: Seismic tomography, mantle petrology, and tectonic evolution. Geosphere 5, 23–50

Boyce, A., Bastow, I., Cottaar, S., Kounoudis, R., Guilloud De Courbeville, J., Caunt, E., et al. (2021). Afrp20: New p-wavespeed model for the african mantle reveals two whole-mantle plumes below east africa and neoproterozoic modification of the tanzania craton. Geochemistry, Geophysics, Geosystems 22, e2020GC009302. doi:https://doi.org/10.1029/2020GC009302

Breiman, L. (2001). Random forests. Machine learning 45, 5–32

Buitinck, L., Louppe, G., Blondel, M., Pedregosa, F., Mueller, A., Grisel, O., et al. (2013). API design for machine learning software: experiences from the scikit-learn project. In ECML PKDD Workshop: Languages for Data Mining and Machine Learning. 108–122

Burton-Johnson, A., Dziadek, R., and Martin, C. (2020). Geothermal heat flow in antarctica: current and future directions. The Cryosphere 14, 3843–3873

Celli, N. L., Lebedev, S., Schaeffer, A. J., and Gaina, C. (2020a). African cratonic lithosphere carved by mantle plumes. Nature communications 11, 1–10

Celli, N. L., Lebedev, S., Schaeffer, A. J., Ravenna, M., and Gaina, C. (2020b). The upper mantle beneath the south atlantic ocean, south america and africa from waveform tomography with massive data sets. Geophysical Journal International 221, 178–204. doi:https://doi.org/10.1093/gji/ggz574

de Wit, M. J., Jones, M. G., and Buchanan, D. L. (1992). The geology and tectonic evolution of the pietersburg greenstone belt, south africa. Precambrian Research 55, 123–153

Ebbing, J., Haas, P., Ferraccioli, F., Pappa, F., Szwillus, W., and Bouman, J. (2018). Earth tectonics as seen by goce-enhanced satellite gravity gradient imaging. Scientific reports 8, 1–9. doi:https://doi.org/10.1038/s41598-018-34733-9

Ebinger, C., Bechtel, T., Forsyth, D., and Bowin, C. (1989). Effective elastic plate thickness beneath the east african and afar plateaus and dynamic compensation of the uplifts. Journal of Geophysical Research: Solid Earth 94, 2883–2901

Emry, E. L., Shen, Y., Nyblade, A. A., Flinders, A., and Bao, X. (2019). Upper mantle earth structure in africa from full-wave ambient noise tomography. Geochemistry, Geophysics, Geosystems 20, 120–147

Fishwick, S. and Bastow, I. D. (2011). Towards a better understanding of african topography: a review of passive-source seismic studies of the african crust and upper mantle. Geological Society, London, Special Publications 357, 343–371

Förste, C., Bruinsma, S., Flechtner, F., Marty, J.-C., Dahle, C., Abrykosov, O., et al. (2013). Eigen-6c2-a new combined global gravity field model including goce data up to degree and order 1949 of gfz potsdam and grgs toulouse. In EGU general assembly conference abstracts. EGU2013–4077

Fullea, J., Lebedev, S., Martinec, Z., and Celli, N. (2021). Winterc-g: mapping the upper mantle thermochemical heterogeneity from coupled geophysical–petrological inversion of seismic waveforms, heat flow, surface elevation and gravity satellite data. Geophysical Journal International 226, 146–191. doi:https://doi.org/10.1093/gji/ggab094

Gard, M. and Hasterok, D. (2021). A global curie depth model utilising the equivalent source magnetic dipole method. Physics of the Earth and Planetary Interiors 313, 106672. doi:https://doi.org/10.1016/j.pepi.2021.106672

Gard, M., Hasterok, D., and Halpin, J. A. (2019). Global whole-rock geochemical database compilation. Earth System Science Data 11, 1553–1566. doi:https://doi.org/10.5194/essd-11-1553-2019

Guyon, I., Weston, J., Barnhill, S., and Vapnik, V. (2002). Gene selection for cancer classification using support vector machines. Machine learning 46, 389–422

Hansen, S. E. and Nyblade, A. A. (2013). The deep seismic structure of the ethiopia/afar hotspot and the african superplume. Geophysical Journal International 194, 118–124

Harris, C. R., Millman, K. J., van der Walt, S. J., Gommers, R., Virtanen, P., Cournapeau, D., et al. (2020). Array programming with NumPy. Nature 585, 357–362. doi:10.1038/s41586-020-2649-2

He, J., Li, K., Wang, X., Gao, N., Mao, X., and Jia, L. (2022). A machine learning methodology for predicting geothermal heat flow in the bohai bay basin, china. Natural Resources Research , 1–24

Head, T., MechCoder, G. L., and Shcherbatyi, I. e. a. (2018). scikit-optimize/scikit-optimize: v0.5.2. Zenodo doi:https://doi.org/10.5281/zenodo.1207017

Hosseini, K., Sigloch, K., Tsekhmistrenko, M., Zaheri, A., Nissen-Meyer, T., and Igel, H. (2020). Global mantle structure from multifrequency tomography using p, pp and p-diffracted waves. Geophysical Journal International 220, 96–141. doi:https://doi.org/10.1093/gji/ggz394

Ince, E. S., Barthelmes, F., Reißland, S., Elger, K., Förste, C., Flechtner, F., et al. (2019). Icgem–15 years of successful collection and distribution of global gravitational models, associated services, and future plans. Earth System Science Data 11, 647–674. doi:https://doi.org/10.5194/essd-11-647-2019

Jaupart, C., Mareschal, J., and Schubert, G. (2007). Heat flow and thermal structure of the lithosphere. Treatise on geophysics 6, 217–252

Kwaya, M. Y., Kurowska, E., Arabi, A. S., et al. (2016). Geothermal gradient and heat flow in the nigeria sector of the chad basin, nigeria. Computational Water, Energy, and Environmental Engineering 5, 70

Lesquer, A. and Vasseur, G. (1992). Heat-flow constraints on the west african lithosphere structure. Geophysical research letters 19, 561–564

Li, M., Huang, S., Dong, M., Xu, Y., Hao, T., Wu, X., et al. (2022). Prediction of marine heat flow based on the random forest method and geological and geophysical features. Marine Geophysical Research 42, 30

Liu, F. T., Ting, K. M., and Zhou, Z.-H. (2008). Isolation forest. In 2008 eighth ieee international conference on data mining (IEEE), 413–422

Lösing, M. and Ebbing, J. (2021). Predicting geothermal heat flow in antarctica with a machine learning approach. Journal of Geophysical Research: Solid Earth 126, e2020JB021499

Lösing, M., Ebbing, J., and Szwillus, W. (2020). Geothermal heat flux in antarctica: assessing models and observations by bayesian inversion. Frontiers in Earth Science 8, 105

Lucazeau, F. (2019). Analysis and mapping of an updated terrestrial heat flow data set. Geochemistry, Geophysics, Geosystems 20, 4001–4024. doi:https://doi.org/10.1029/2019GC008389

Meyer, B., Saltus, R., and Chulliat, A. (2017). Emag2 version 3-update of a two arc-minute global magnetic anomaly grid. In EGU General Assembly Conference Abstracts. 10614. doi:https://doi.org/10.7289/V5H70CVX

Muller, M., Jones, A., Evans, R., Grütter, H., Hatton, C., Garcia, X., et al. (2009). Lithospheric structure, evolution and diamond prospectivity of the rehoboth terrane and western kaapvaal craton, southern africa: Constraints from broadband magnetotellurics. Lithos 112, 93–105

Pail, R., Goiginger, H., Schuh, W.-D., Höck, E., Brockmann, J. M., Fecher, T., et al. (2010). Combined satellite gravity field model goco01s derived from goce and grace. Geophysical Research Letters 37

[Dataset] pandas development team, T. (2020). pandas-dev/pandas: Pandas. doi:10.5281/zenodo.3509134

Rezvanbehbahani, S., Stearns, L. A., Kadivar, A., Walker, J. D., and van der Veen, C. J. (2017). Predicting the geothermal heat flux in greenland: A machine learning approach. Geophysical Research Letters 44, 12–271

Rimi, A. (2000). First assessment of geothermal resources in morocco. In Proceedings of the World Geothermal Congress. 397–402

Rogers, N., Macdonald, R., Fitton, J. G., George, R., Smith, M., and Barreiro, B. (2000). Two mantle plumes beneath the east african rift system: Sr, nd and pb isotope evidence from kenya rift basalts. Earth and Planetary Science Letters 176, 387–400

Schaeffer, A. and Lebedev, S. (2013). Global shear speed structure of the upper mantle and transition zone. Geophysical Journal International 194, 417–449. doi:https://doi.org/10.1093/gji/ggt095

Schaeffer, A. and Lebedev, S. (2015). Global heterogeneity of the lithosphere and underlying mantle: A seismological appraisal based on multimode surface-wave dispersion analysis, shear-velocity tomography, and tectonic regionalization. In The Earth's heterogeneous mantle (Springer). 3–46

Sengör, A. C. and Burke, K. (1978). Relative timing of rifting and volcanism on earth and its tectonic implications. Geophysical Research Letters 5, 419–421

Shahdi, A., Lee, S., Karpatne, A., and Nojabaei, B. (2021). Exploratory analysis of machine learning methods in predicting subsurface temperature and geothermal gradient of northeastern united states. Geothermal Energy 9, 1–22

Shapiro, N. M. and Ritzwoller, M. H. (2004). Inferring surface heat flux distributions guided by a global seismic model: particular application to antarctica. Earth and Planetary Science Letters 223, 213–224

Siebert, L., Cottrell, E., Venzke, E., and Andrews, B. (2015). Earth's volcanoes and their eruptions: An overview. In The Encyclopedia of Volcanoes (Elsevier). 239–255. doi:10.1016/b978-0-12-385938-9.00012-2

Sobh, M., Ebbing, J., Mansi, A. H., Götze, H.-J., Emry, E., and Abdelsalam, M. (2020). The lithospheric structure of the saharan metacraton from 3-d integrated geophysical-petrological modeling. Journal of Geophysical Research: Solid Earth 125, e2019JB018747

Sobh, M., Gerhards, C., Fadel, I., and Götze, H.-J. (2021). Mapping the thermal structure of southern africa from curie depth estimates based on wavelet analysis of magnetic data with uncertainties. Geochemistry, Geophysics, Geosystems 22, e2021GC010041

Stål, T. and Reading, A. M. (2019). A grid for multidimensional and multivariate spatial representation and data processing. doi:http://doi.org/10.5334/jors.287

Stål, T., Reading, A. M., Halpin, J. A., and Whittaker, J. M. (2021). Antarctic geothermal heat flow model: Aq1. Geochemistry, Geophysics, Geosystems 22, e2020GC009428

Thorpe, R. and Smith, K. (1974). Distribution of cenozoic volcanism in africa. Earth and Planetary Science Letters 22, 91–95

[Dataset] Uieda, L., Tian, D., Leong, W. J., Jones, M., Schlitzer, W., Toney, L., et al. (2021). PyGMT: A Python interface for the Generic Mapping Tools. doi:10.5281/zenodo.5607255

Virtanen, P., Gommers, R., Oliphant, T. E., Haberland, M., Reddy, T., Cournapeau, D., et al. (2020). SciPy 1.0: Fundamental Algorithms for Scientific Computing in Python. Nature Methods 17, 261–272. doi:10.1038/s41592-019-0686-2

Waskom, M. L. (2021). seaborn: statistical data visualization. Journal of Open Source Software 6, 3021. doi:10.21105/joss.03021

Supplementary Material for "A geothermal heat flow model for Africa based on Random Forest Regression"

1 SUPPLEMENTARY FIGURES

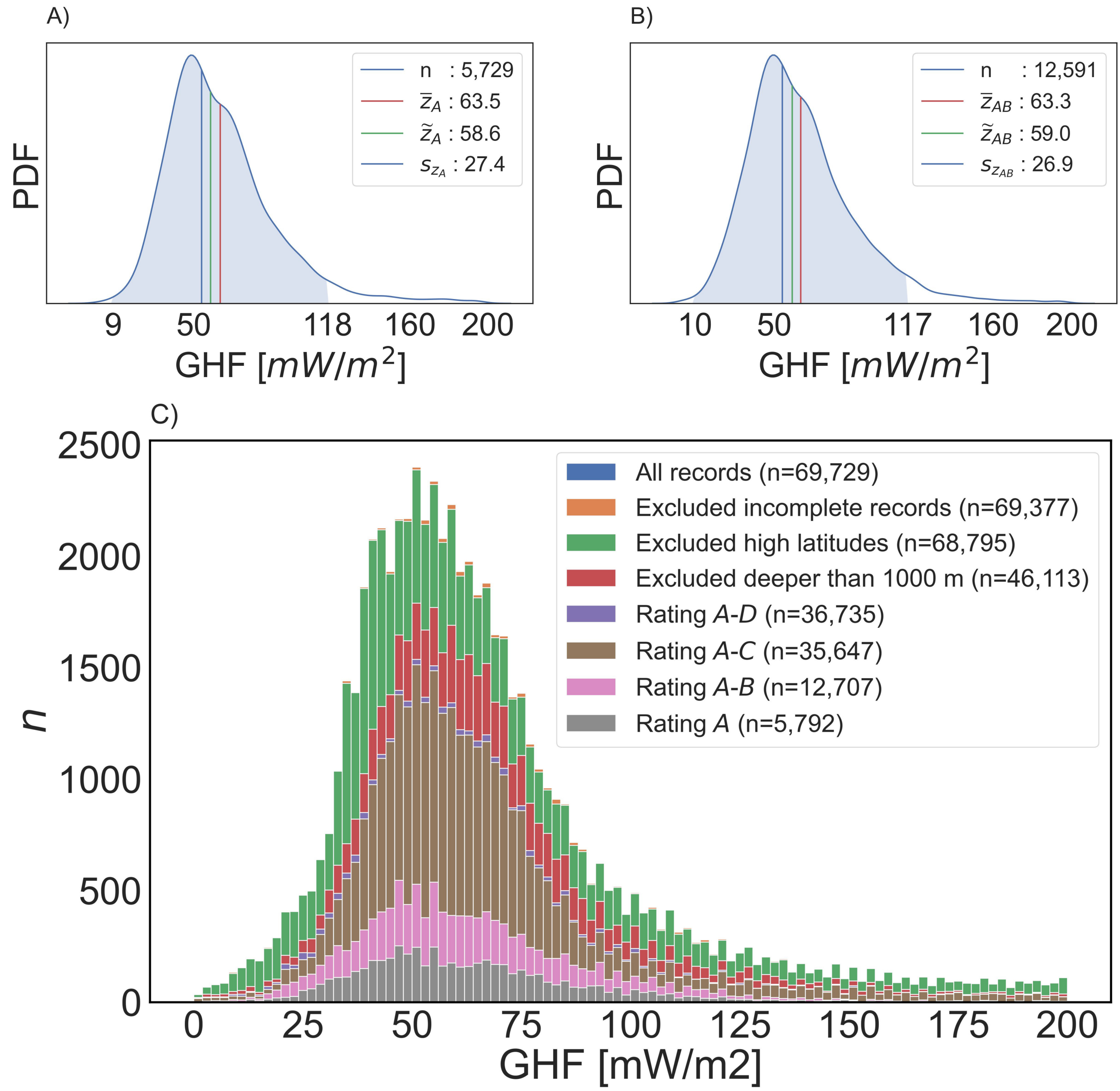

Figure S1. (A) Density plot of global GHF measurements labeled A without questionable values, (B) Density plot of global GHF measurements labeled A and B without questionable values, (C) Histogram of global binned GHF measurements with all records, records after removal of incomplete information, records after removal of high latitude and of deep-sea information, and records labeled with different quality in the NGHF database (Lucazeau, 2019). $\bar{z}$ = mean, $\tilde{z}$ = median, s = standard deviation.

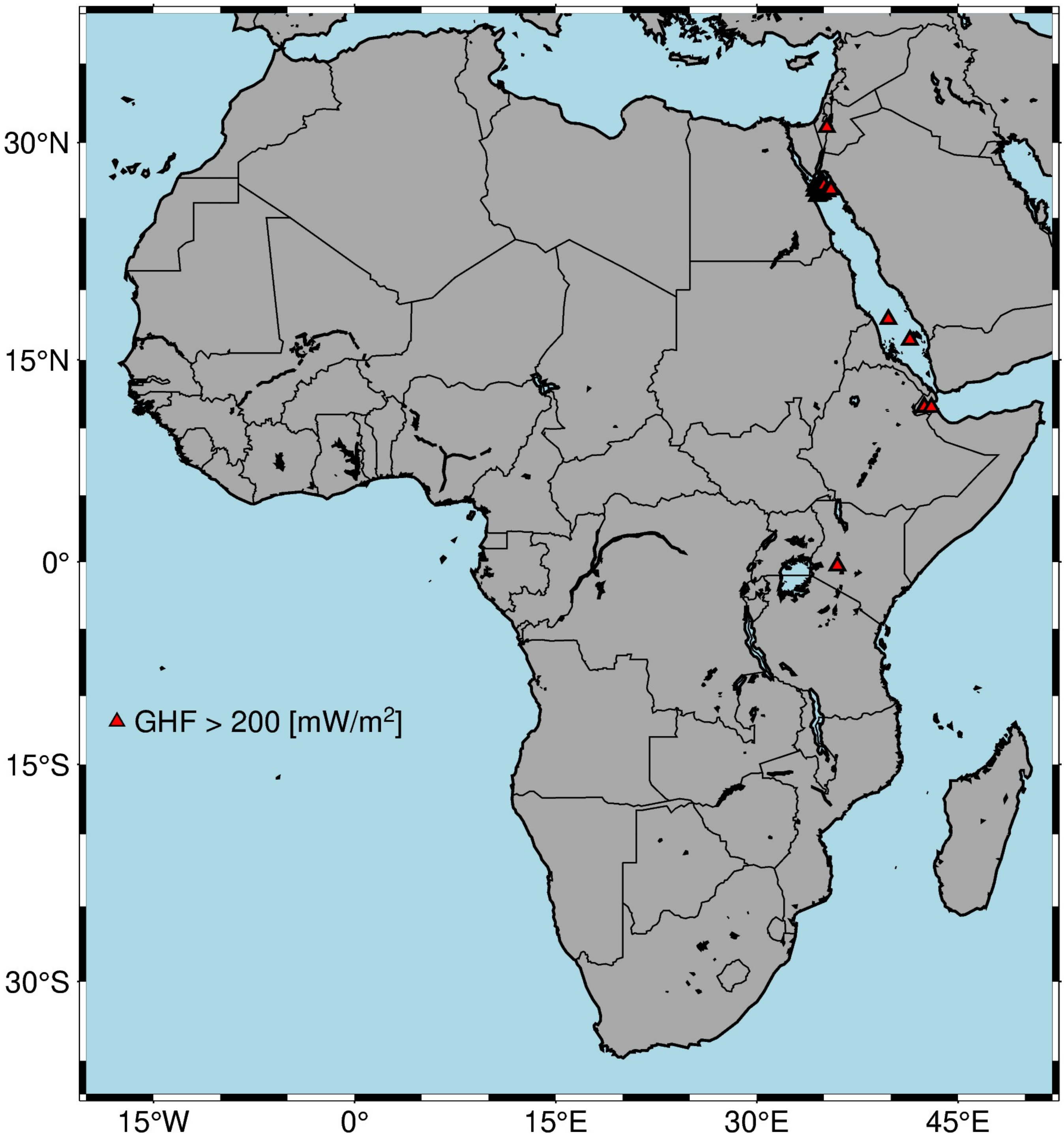

Figure S2. Locations of GHF measurements > 200 mWm^{-2} (Lucazeau, 2019).

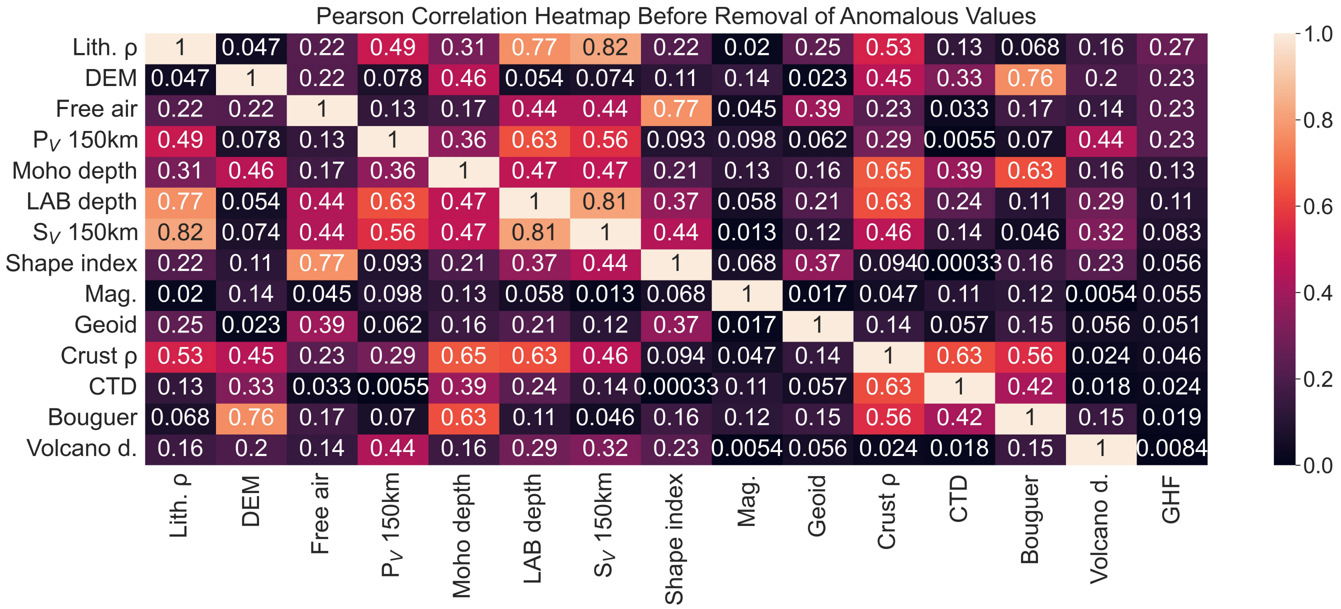

Figure S3. Pearson correlation matrix between observables and GHF reference data, before removing anomalous values; ranked by decreasing correlation with GHF.

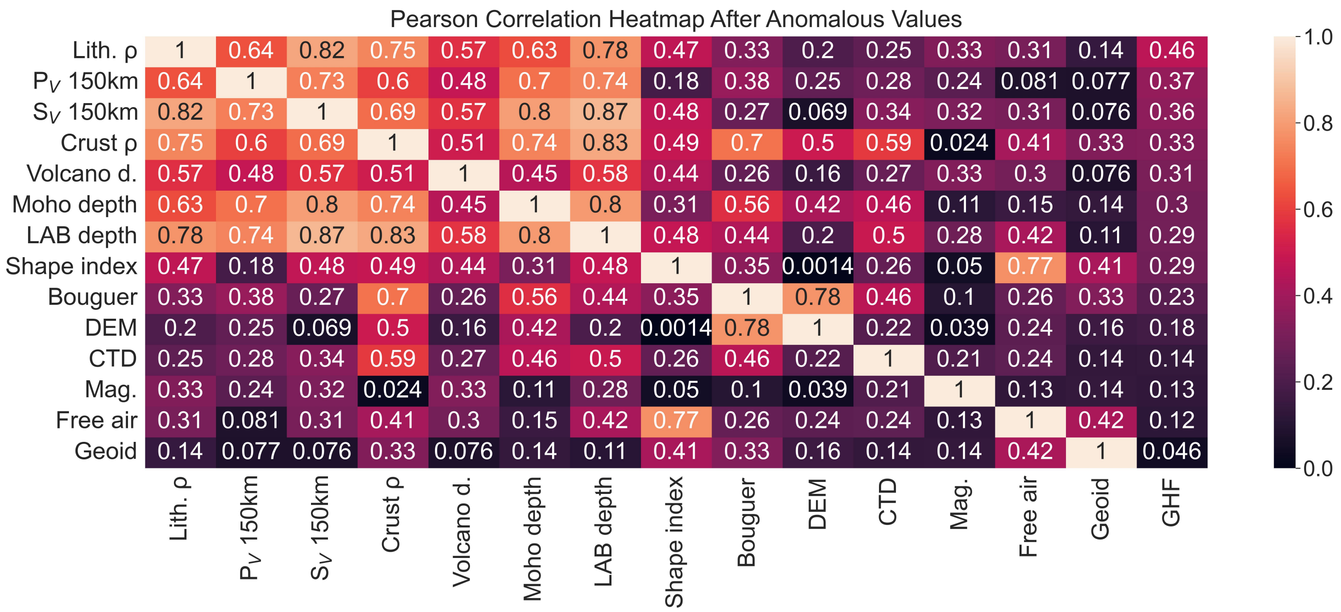

Figure S4. Pearson correlation matrix between observables and GHF reference data, after removing anomalous values; ranked by decreasing correlation with GHF.

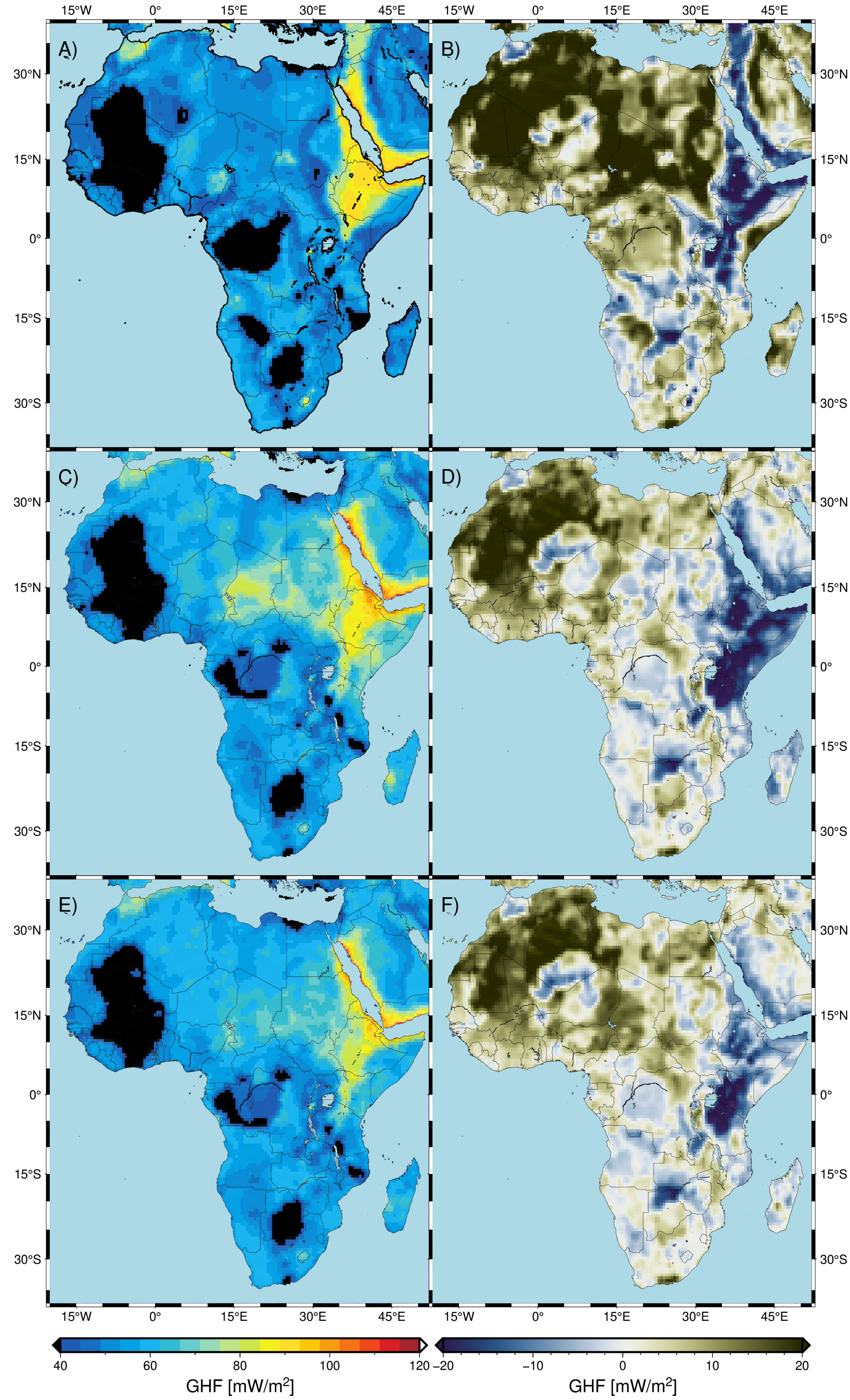

Figure S5. AFQ models trained with reference GHF data labeled *A* and different numbers of observables: (A) AFQ model trained with four observables, (B) Residual between optimal AFQ model trained with eleven observables and AFQ trained with four observables, (C) AFQ model trained with nine observables, (D) Residual between optimal AFQ model trained with eleven observables and AFQ trained with nine observables, (E) AFQ model trained with all sixteen observables, (F) Residual between optimal AFQ model trained with eleven observables and AFQ trained with all sixteen observables.

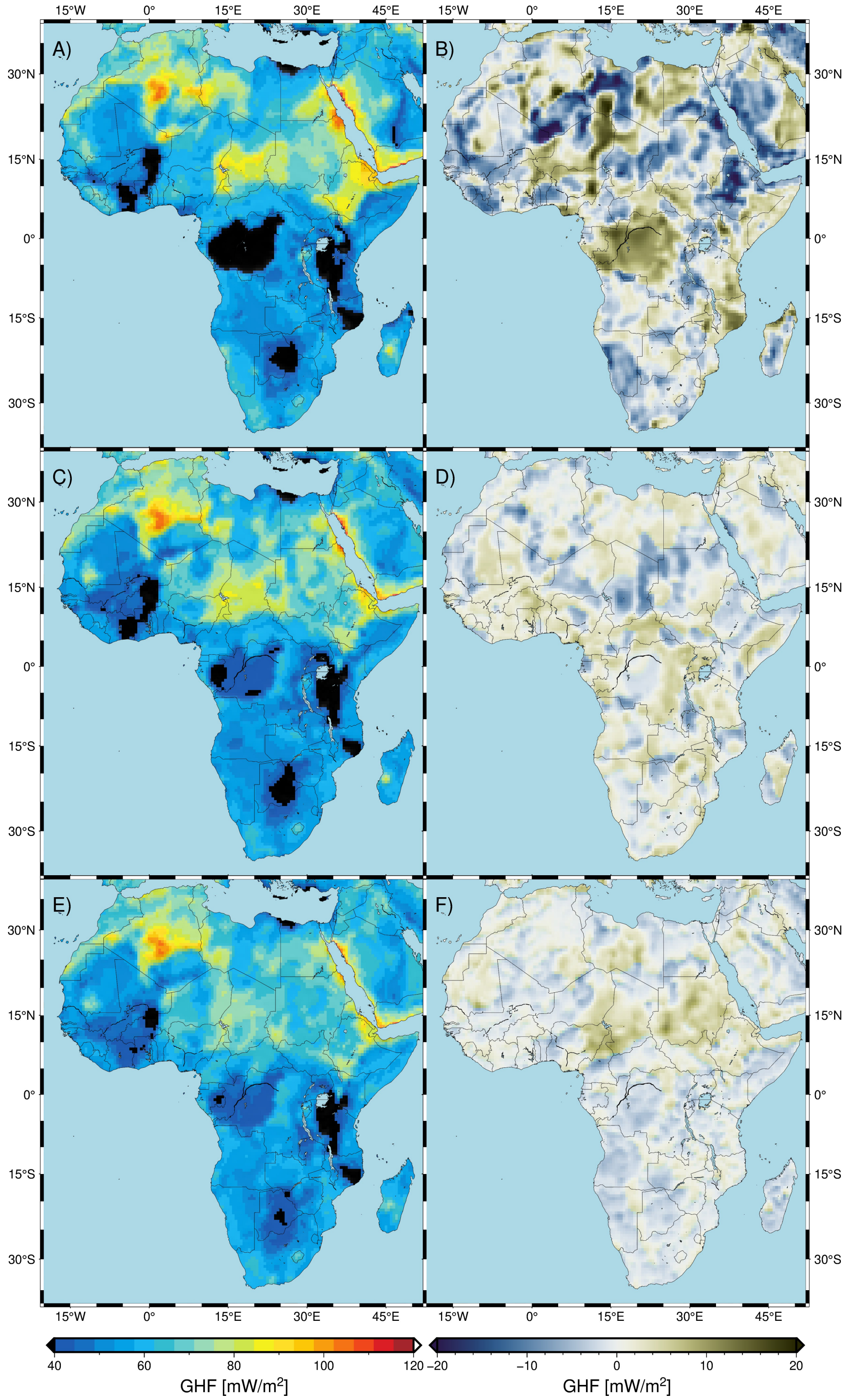

Figure S6. AFQ models trained with reference GHF data labeled *A* and *B* and different numbers of observables: (A) AFQ model trained with four observables, (B) Residual between optimal AFQ model trained with eleven observables and AFQ trained with four observables, (C) AFQ model trained with nine observables, (D) Residual between optimal AFQ model trained with eleven observables and AFQ trained with nine observables, (E) AFQ model trained with all sixteen observables, (F) Residual between optimal AFQ model trained with eleven observables and AFQ trained with all sixteen observables.

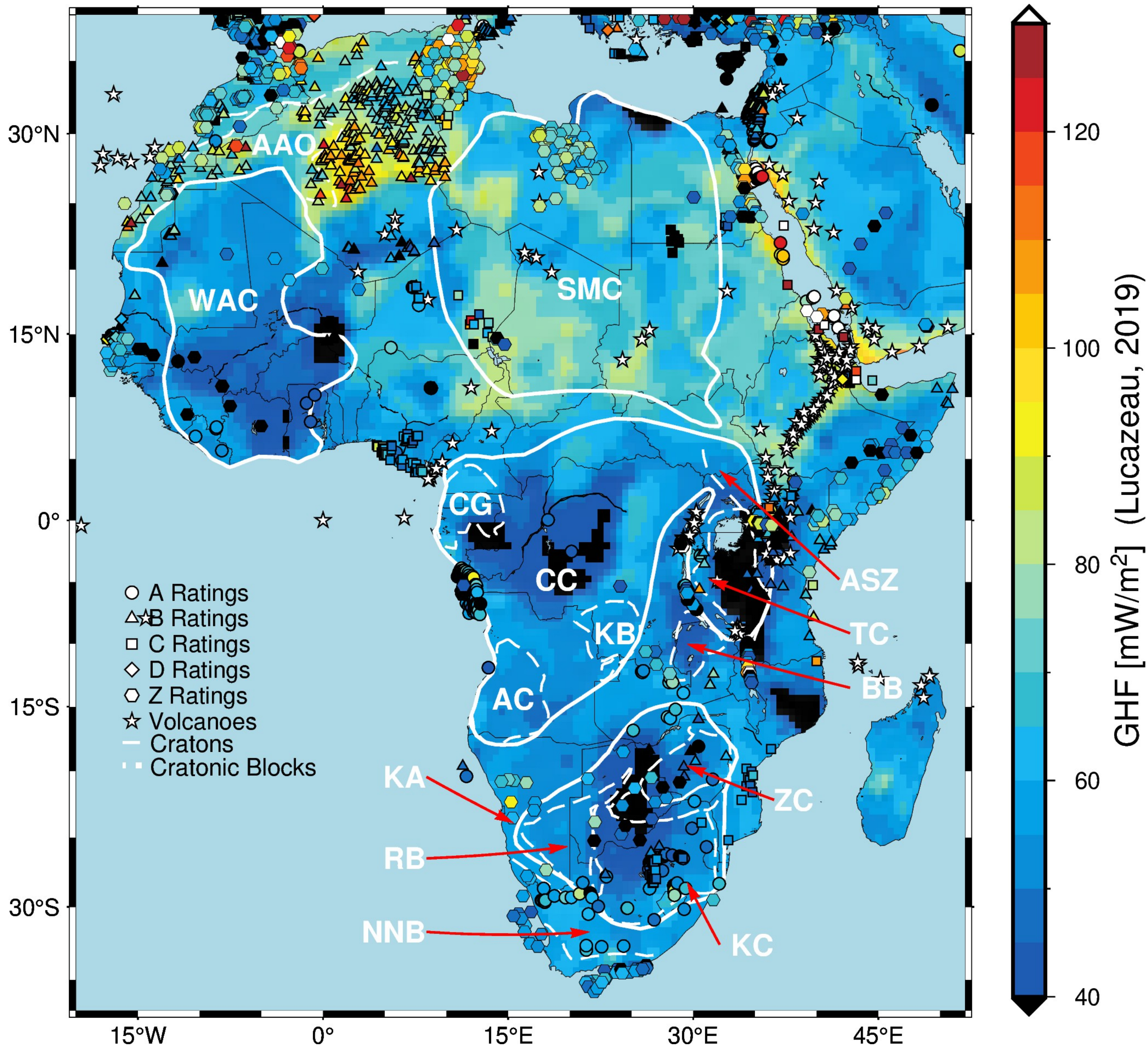

Figure S7. AFQ model trained with eleven observables, overlain with the tectonic map of Africa as well as GHF measurements. Cratons are plotted in white polygons, KA = Kalahari Craton; CC = Congo Craton; WAC = West African Craton; SMC = Saharan Metacraton. Cratonic blocks: BB = Bangweulu Block; ZC = Zimbabwe Craton; TC = Tanzanian Craton; KC = Kaapvaal Craton; AC = Angola Craton; KB = Kasai Block; GC = Gabon–Cameroon Block. RB = Rehoboth Block; NNB = Namaqua-Natal Belt; ASZ = Aswa Shear Zone. Symbols of circle, triangle, square, diamond and hexagon represent the Reference GHF with A, B, C, D and Z ratings respectively, derived from global compilation of GHF database (Lucazeau, 2019). White asterisks = Volcanoes.

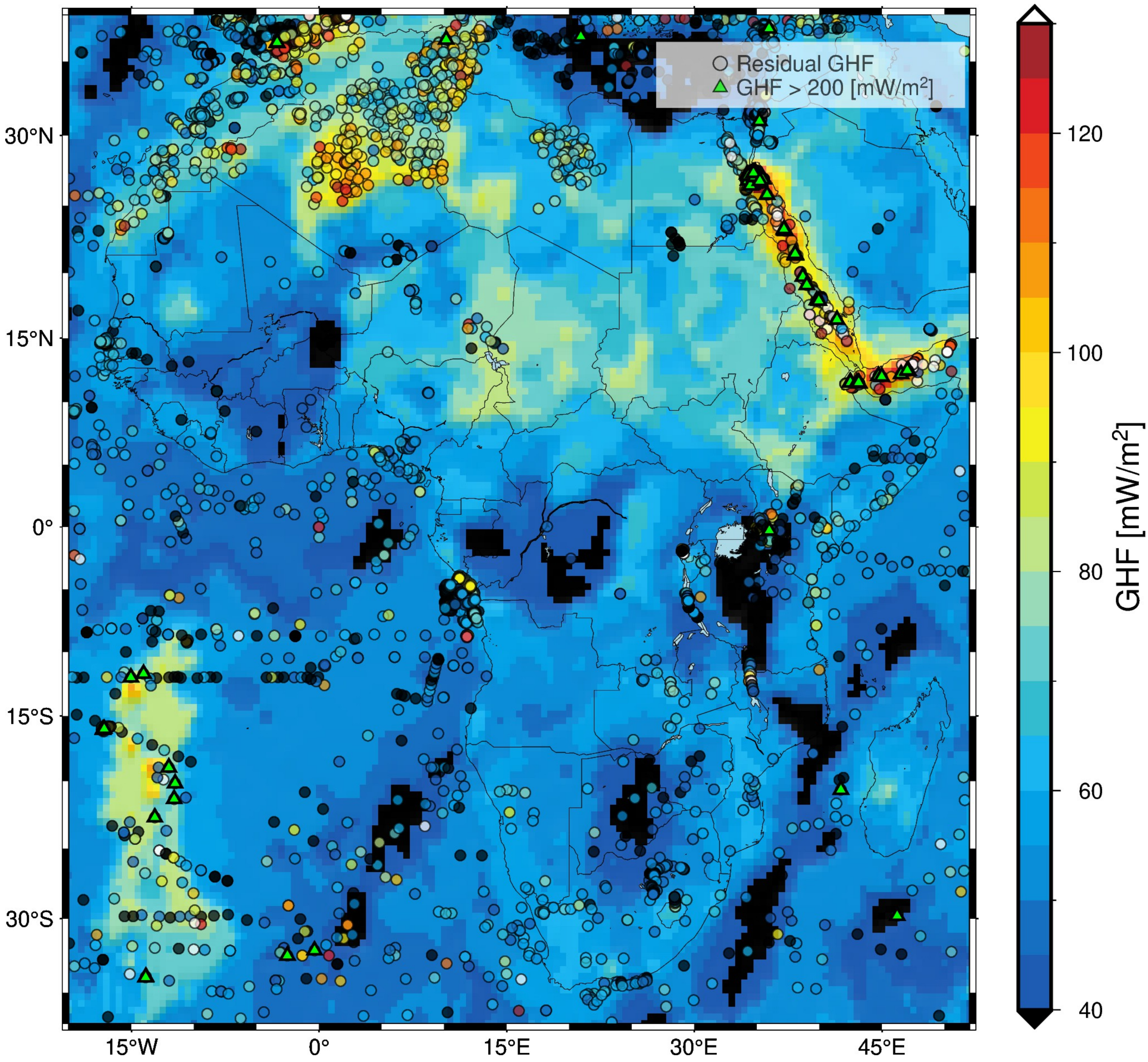

Figure S8. AFQ model trained with eleven observables including oceanic GHF. Circle represents the GHF labeled A, B, C, D and Z, as well as deep-sea measurements derived from the global compilation of heat flow databases (Lucazeau, 2019).

REFERENCES

Lucazeau, F. (2019). Analysis and mapping of an updated terrestrial heat flow data set. Geochemistry, Geophysics, Geosystems 20, 4001–4024. doi:https://doi.org/10.1029/2019GC008389